designs

MDPI

Article

Design and Calibration of a 3D-Printed Cup-Vane Wireless Sensor Node

Samuel Kang'iri [1,*], Christian Gradl [2], Jean Byiringiro [1] and Harrison Ngetha [3]

[1] Department of Mechatronic Engineering, Dedan Kimathi University of Technology, 10100 Nyeri, Kenya; jean.bosco@dkut.ac.ke
[2] Department of Chemical and Biological Engineering, Friedrich-Alexander-Universitat, 91054 Erlangen, Germany; batzn@web.de
[3] Department of Electrical and Electronic Engineering, Dedan Kimathi University of Technology, 10100 Nyeri, Kenya; harrison.ngetha@dkut.ac.ke
* Correspondence: samuel.macharia@dkut.ac.ke; Tel.: +254-726-240-861

Received: 14 May 2018; Accepted: 14 June 2018; Published: 21 June 2018

Abstract: There has been constant growth in the wind energy market. A study conducted in January 2018 by Global Market Insights Inc. predicted that the global wind energy market will surpass USD 170 billion by 2024. Before installation of a wind turbine, wind data must be collected from a prospective site for a minimum of one year. This has compelled the high demand for instruments used for collecting wind data. Various commercial cup anemometers and wind vanes have been manufactured for sale, some of which lack proper calibration or are not affordable for small-scale wind farmers, especially in developing countries. Wind data are a big data affair and call for instruments that handle them as such, unlike most commercial wind data collection instruments. This paper presents the design and calibration of a wireless 3D-printed cup-vane instrument for collecting wind data. This instrument represents a Wireless Sensor Node (WSN) in the Internet of Things (IoT). This study gave rise to an instrument system that was able to acquire wind data within a mean fitting deviation of ± 0.063398 m/s, store them and present them wirelessly to an IEEE 802.15.4 protocol sink node. This was verified in the lab using 1 m/s to 16 m/s wind speeds at the Armfield^{TM} wind tunnel and outside in an open field with 1 m/s to 5 m/s wind speeds.

Keywords: wind data; wireless sensor node; 3D-printing; big data; Internet of Things; cup-vane

1. Introduction

Wind energy farming is a non-polluting alternative to fossil fuels. It does not involve burning of fossil fuels, an exercise that contributes to global warming [1]. Countries around the globe have continued to invest in wind energy. China has become the world's largest electricity generator from wind energy with around 188 GW by 2017 [2]. Kenya launched a 310 MW wind power project in 2016, which became the largest wind farm in Africa [3,4].

At the beginning of a wind turbine project, wind data must be collected for at least one year to capture the wind speed and seasonal variations in direction. There are various instruments that can be used to measure wind speed. In reference to [5–7], these instruments may include the following:

1. Velocity anemometers

   These include cup anemometers, windmill anemometers, hot-wire anemometers, Laser Doppler anemometers, sodar and LiDAR anemometers and ping-pong ball anemometers.
2. Pressure anemometers

   These include plate anemometers and tube anemometers.

Despite the recent growth of sodar and LiDAR anemometers, from the above listed instruments, the cup anemometer is widely accepted as the standard instrument for measuring wind speed [8–11]. Among other attractive advantages, L.Kristensen [12] stated that, 'experience has shown that the cup anemometer is a robust and reliable instrument which can operate unattended for years'. Companies such as Ammonit™ have specialized in making cup anemometers and wind vanes [13] and have emerged among the best in serving the wind data collection market. These companies are well established in the market and serve most large-scale wind power projects. However, most small-scale wind farmers in developing countries do not have access to well-calibrated high-end instruments, and this frustrates small-scale wind farmers. In addition, most wind data collection instruments are not able to collect wind data in a way that can be networked with others to deliver big data to a common Internet of Things pool, ready for analysis and prediction. This study strives to close this gap.

2. Literature Review

2.1. Cup and Vane Instrument Design

Taking a look at the design of the cup anemometer, since its invention by T. R. Robinson in 1846 [14], the greatest interest in the cup anemometer design was only its linearity. Even though further studies have shown that it is actually 'almost linear', the calibration of the cup anemometer is highly linear [12]. This is still an attractive feature that makes the calibration process easy and reliable. However, from the year 1920, this linearity feature of interest has shifted to the over-speeding nature of the cup anemometer. As explained by L. Kristensen et al. [15], over-speeding of cup anemometers is a characteristic effect caused by the fact that cup anemometers tend to respond more to an increase in speed than to breaking. This is commonly known as the asymmetric response of the cup anemometers. This may be perceived to be a negative feature, but it is actually a property that allows the cup anemometer to start off.

For wind vane design, J. Wieringa [16] showed wind vane motion described by the damping ratio, natural wavelength and decay distance to be insufficiently described by a second order equation. This was as a result of the torque changes with a change in the angle of attack. With measured vane dimensions, a relationship was derived between the measured vane dimensions and motion constants. It was shown that with a fin attached to the vane, the motion of the vane is independent of the fin area. In a quest to improve the responsiveness of wind vane direction measurements, Johann et al. [17] developed a mathematical model describing the dynamic behavior of a wind vane. This model was then used to determine the form factor that would have the best response to the disturbances the vane would encounter. Nevertheless, this model was not embodied.

In a related design, Hsiao et al. [18] proposed a power harvester mechanism integrating solar radiation and wind power harvesting. The pyroelectric effect was used in harvesting the thermal energy from solar radiation, while a disk generator was used to harness wind energy. This demonstrated a novel integrated energy harvester design that is complementary and useful in energy fluctuation management.

2.2. 3D Printing

3D printing has been embraced by every sector involved in manufacturing. As recorded, 3D printing lowers the cost of manufacturing, improves efficiency, and brings about high flexibility [19]. It has been predicted that the 3D-printed parts market will grow to an 8.4 billion dollar industry by 2025 [20]. At an advanced level, 3D-printing technology is being used to print electronic devices, as well as their casings. Yuanyuan et al. [21] showed a significant growth and advancement in 3D printing technology for the manufacturing of sensors. An exact sensor is printed with the exact specifications as needed in its application.

For small batches, 3D printing introduces fabrication freedom by making products with exact specifications as required [22]. In the 2016 Global Congress on Manufacturing and Management, Phani et al. [23] explained how mass customization of products and services is becoming preferred

over mass production. The current global diversification and existence of unpredictable market trends is pushing manufacturing to its limits. Unlike the traditional manufacturing technologies, digital manufacturing is a promising technology that fits the current dynamic market trends.

As discussed by Octavio et al. [24], when designing, it is important to achieve a cost-effective and environmentally-efficient process. With the aim of reducing oil emulsion-type coolants used during machining of aeronautical engine components, they designed two nozzle adaptors and tested various geometries using computational fluid dynamics (CFD). Finally, they tested it as a CryoMQL demonstrator in comparison with other techniques. Their method was able to balance the technical and environmental issues.

2.3. Cost-Effective Data Acquisition Systems

Amar Adane et al. [25] presented a microcontroller-based data acquisition system that was able to automatically get sensor data from the station. The acquired data were transferred to a computer through a serial connection and then analyzed. For large-scale wind farm applications, Neha and Kumar [26] worked on a wireless Supervisory Control and Data Acquisition (SCADA) system that monitored and collected the required data parameters remotely. General Packet Radio Service (GPRS) was utilized in sending data packets from the remote location. Eftichiof and Kostas [27] described a similar system, but more cost-effective in the sense that it was based on a simple microcontroller. This microcontroller was interfaced with sensors to collect data and deliver them to the computer via RS-232 connection. However, these methods did not offer the required wireless networking capabilities.

Chin and Tan [28] discussed a wireless sensor network method. A star node network of six sensors based on XBee was used to collect data from different remote locations. The data were then sent to a data logger through a gateway from each node. These data were then processed and uploaded to the Internet via the Global System for Mobile communications (GSM) network for further processing. Nisha and Versha [29] discussed a notably similar method, built around a cost-effective microcontroller. SriLakshmi et al. [30] discussed a wireless data collection method based on the ESP8266 module that uses the IEEE 802.11 protocol. The collected data were sent wirelessly from up to a distance of 30 m. This method was however not sufficient for wind resource assessment, given that the wind data measurement mast could go up to 100 m. In an attempt to close the discussed gaps, this study presents the design and calibration of a 3D-printed cup-vane wireless sensor node that facilitate big wind data collection for the ease of Internet of Things integration.

3. Design of the Cup-Vane and Wireless Sensor Node Instrument

3.1. Cup-Vane Design

The first criteria for the design of the cup-vane instrument was its geometry. Calibration of the cup anemometer depends on its rotor geometry. To maximize the air flow separation, it is desirable that the cups of the cup-vane instrument be conical. Light cup anemometers are least prone to the over-speeding problem. They are also more sensitive to the moving wind. This formed the basis for the second criteria for designing the cups. The design criteria for the vane of the cup-vane instrument were to make the tail blade light and shaped to respond to wind speeds from around 1 m/s to reduce the feathery flipping effect caused by over-sensitivity.

The cup-vane instrument used in this study was designed with the help of Autodesk® Inventor® software, as shown in Figure 1. This design captured the main parts of the cup-vane instrument. However, a body had to be designed to hold together the cup-vane design, as well as the temperature, humidity, pressure and altitude sensors. The cup-vane body was hence designed in consideration of the sensors and the supportive embedded systems that were to be installed. The design presented in Figure 2 shows the virtual assembly of the complete cup-vane instrument.

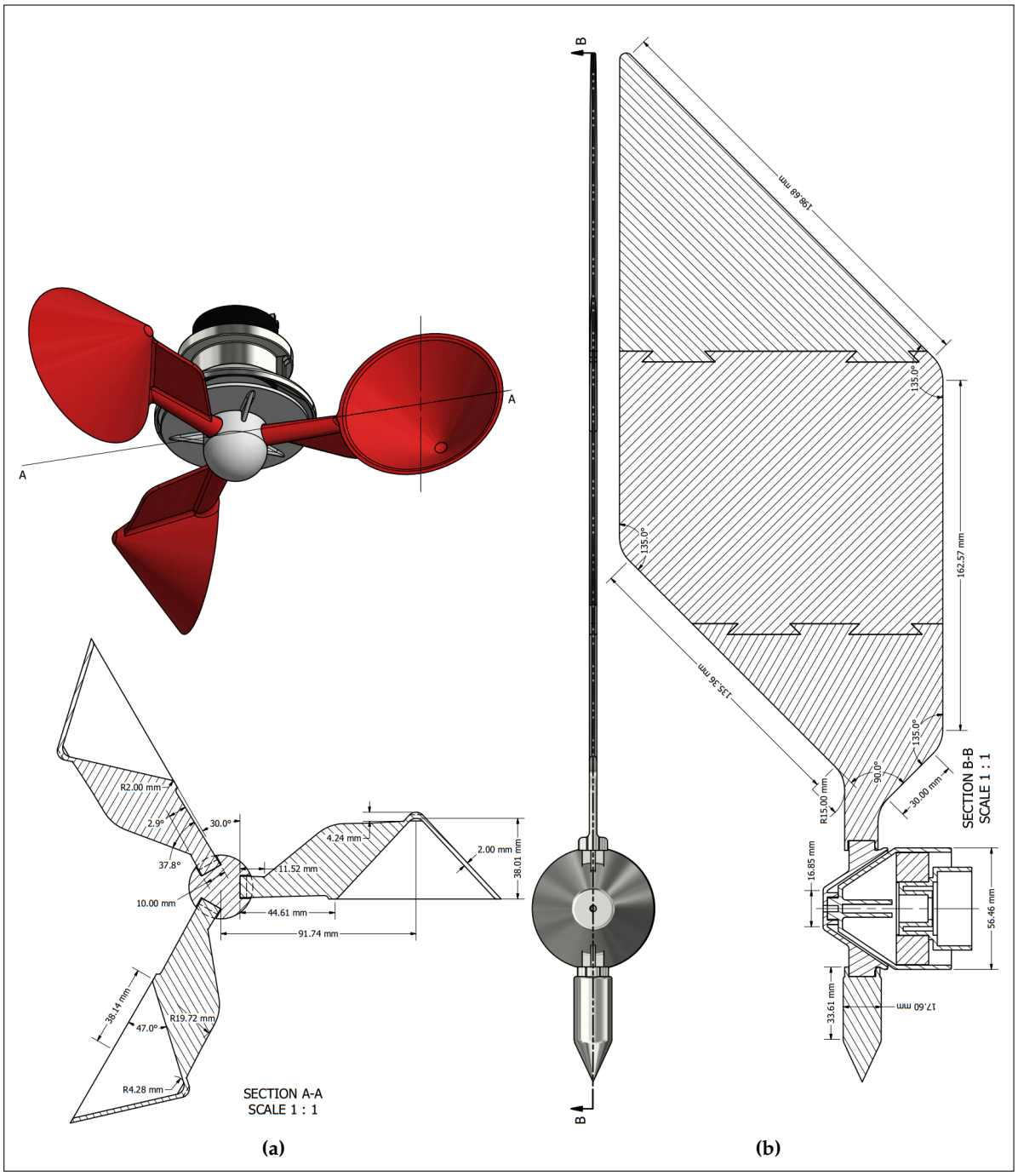

Figure 1. Cup-vane instrument design: (**a**) cup design and its section view (A-A); and (**b**) vane design and its section view (B-B).

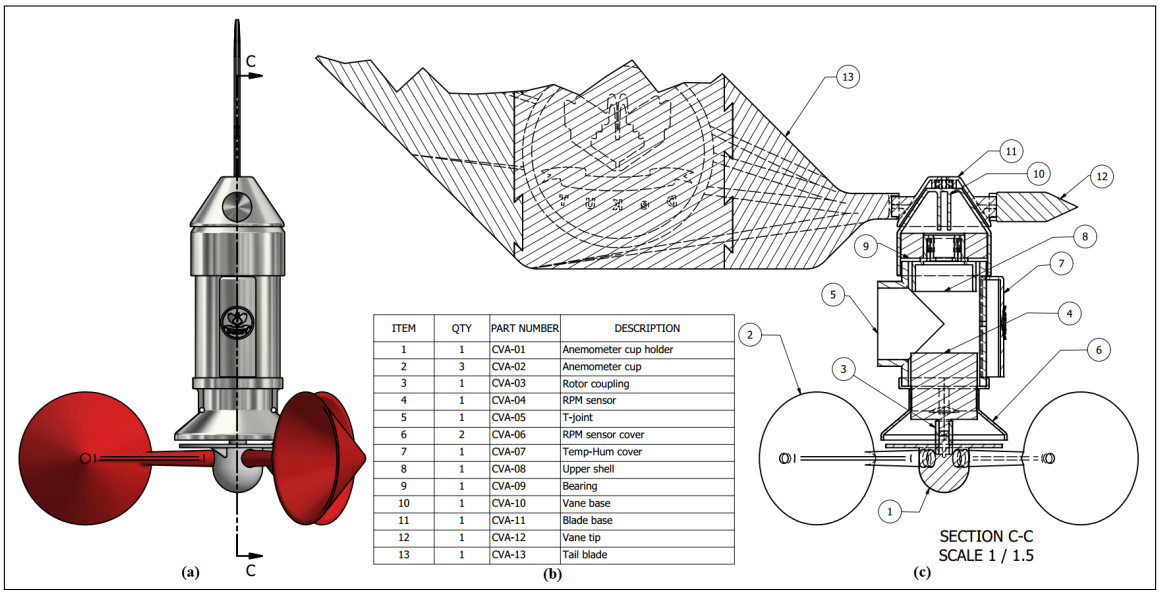

ITEM	QTY	PART NUMBER	DESCRIPTION
1	1	CVA-01	Anemometer cup holder
2	3	CVA-02	Anemometer cup
3	1	CVA-03	Rotor coupling
4	1	CVA-04	RPM sensor
5	1	CVA-05	T-joint
6	2	CVA-06	RPM sensor cover
7	1	CVA-07	Temp-Hum cover
8	1	CVA-08	Upper shell
9	1	CVA-09	Bearing
10	1	CVA-10	Vane base
11	1	CVA-11	Blade base
12	1	CVA-12	Vane tip
13	1	CVA-13	Tail blade

Figure 2. Cup-vane virtual assembly: (**a**) full assembly; (**b**) parts list and (**c**) sectioned view (C-C).

3.2. Embedded Systems Design

The criterion for the embedded system design was to come up with a cost-effective wireless data transmitter in a small form factor. The second criterion was the power consumption. For effective wind data collection from the field, the system needed to be able to operate on available solar power-banks for around one year. The embedded system used in this study was built around the Atmega328P-AU microcontroller. This implementation also had an XBee radio capable of transmitting data via the ZigBee IEEE 802.15.4 protocol, to a central station located up to 100 m away. A simplified representation of the schematic used is shown in Figure 3. The final implementation was a compact PCB enclosed in a 3D-printed case. This system was flashed with a program that facilitated effective sensors data acquisition and transmission. This program is the algorithm discussed in the next subsection.

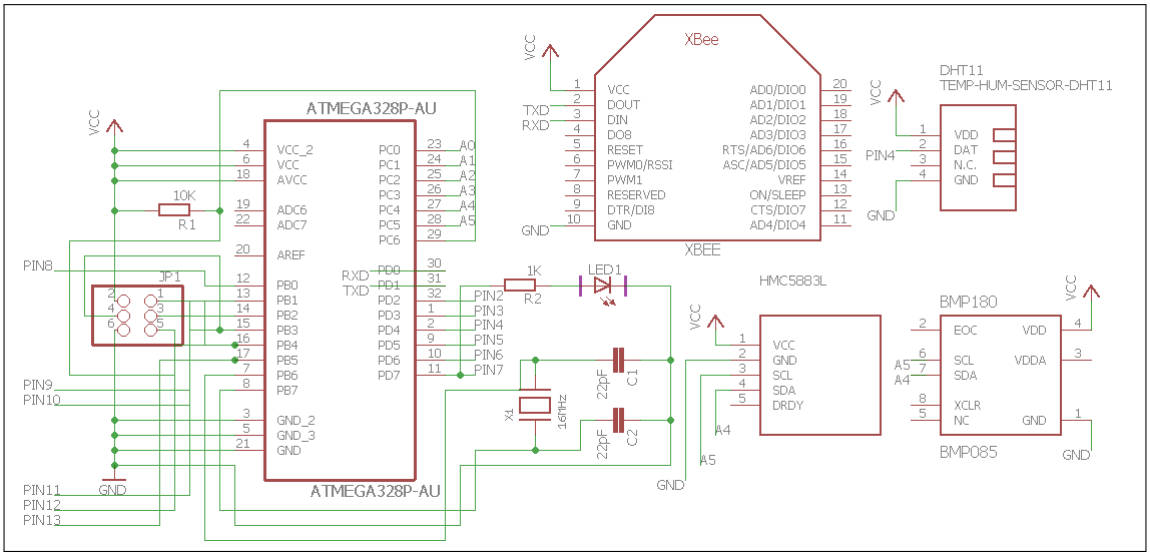

Figure 3. Wireless sensor node electrical schematic diagram.

3.3. Wireless Sensor Node Algorithm

In this study, the main task for the pre-processing algorithm was to prepare the station's embedded systems to collect the data from sensors and send those data to the main post-processing station located far from it. As sampled in Appendix B, this algorithm was prepared in an ANSI C/C++ development environment. To start with, the sensors pins and addresses were defined. Some sensors such as HMC5883L needed to communicate via the Inter-Integrated Circuit (I^2C) protocol. Their addresses were defined, and the required sensor libraries were included in the program.

The necessary setups were prepared inside a function that was only called once. This preparation included specification of the involved sensor interrupt, pulling up the internal resistors and starting up the sensors, as well as the serial communication. The iteration required was done in a one loop function. During the entire iteration, time elapsing was noted by the program. Sensors were configured to collect data samples after every second and transmit the average data samples after five seconds. The sensors' calibration details were considered in this iteration, as well. As illustrated in Algorithm A1 of Appendix B, the speed sensor was prepared to provide current revolutions-per-minute (RPM).

As illustrated in Algorithm A2 of Appendix B, the compass sensor was configured to capture the changes in the direction of the wind vane tail. The declination angle was also taken care of. Similarly, a request to the sensors responsible for reading the temperature, pressure and altitude was made. All the collected sensor data were transmitted in a comma separated format. This is as illustrated in Algorithm A3 of Appendix B. The test IEEE 802.15.4 sink node located 100 m away was able to receive the comma separated data after every five seconds. These data are as presented in Table A6.

3.4. 3D Printing and Assembly

After the Computer-Aided Design (CAD), all the 3D parts were converted to .stl file format ready for 3D printing through Fused Deposition Modeling (FDM). The 3D printing task was performed using the MakerBot™ 3D printer. The individual parts were printed separately, one at a time, waiting to be assembled. The physical setup for the 3D printing exercise was as shown in Figures A1 and A3 in Appendix A. After printing all the cup-vane instrument parts, all the internal sensors were installed as shown in Figure 4. Other sensors such as temperature and altitude sensors were installed in a similar way. This installation exercise included all the wiring needed for every sensor to get power and deliver the data signals.

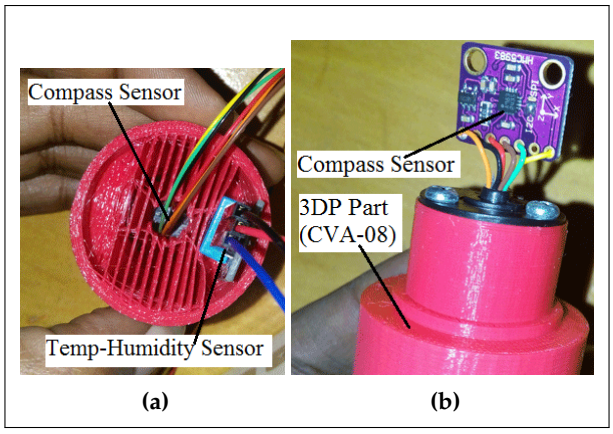

Figure 4. Sensor installation: (**a**) installation process; and (**b**) installed sensor.

The complete installation of the sensors into the cup-vane body is shown in Figure 5a. From this point, the anemometer cups and the wind vane tail blade were installed. The whole assembly was then painted and polished to make a finished cup-vane instrument (see Figure 5b). For this cup-vane instrument to work, it was required that it be interfaced with the developed embedded system.

The embedded system captured the sensors; signals, translated the signals into the required data and transmitted these data to a sink node.

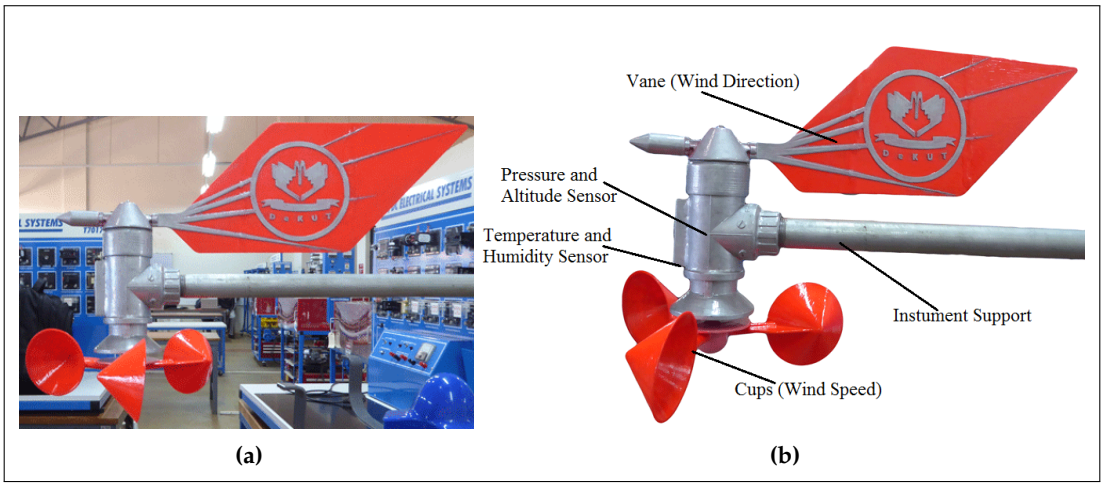

Figure 5. Finished cup-vane instrument: (**a**) lab, all sensors installed; and (**b**) finished assembly.

4. Designed Cup-Vane Instrument Calibration and Analysis

4.1. Cup Calibration Setup

The cup anemometer used in this study was built around the Omron incremental rotary encoder. Its datasheet [31] was used during the construction of the cup anemometer. The setup for cup anemometer calibration was as shown in Figure 6.

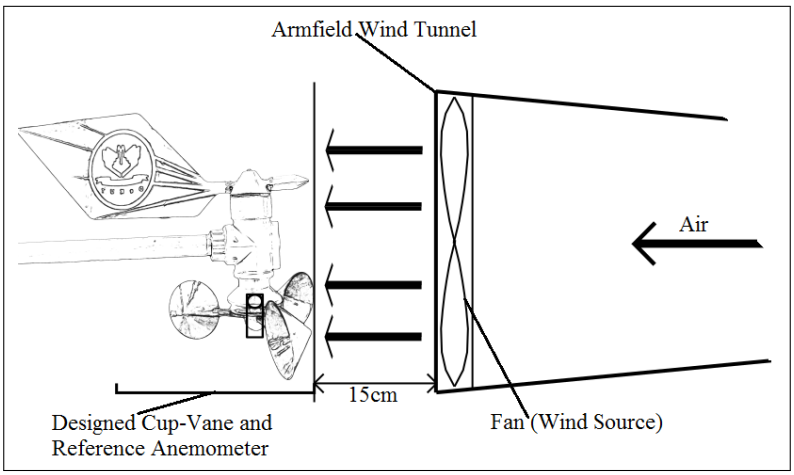

Figure 6. Designed cup-vane calibration setup.

4.2. Cup Calibration Results and Analysis

During this calibration process, the calibration guidelines [11,32,33] were utilized. To compare the designed cup-vane revolutions-per-minute data with the wind speed data from the reference anemometer, the experiment was setup as seen in Figure 6. The results of these measurements' datasets Run (1) and Run (2) seen in Table A1 were plotted as shown in Figure 7.

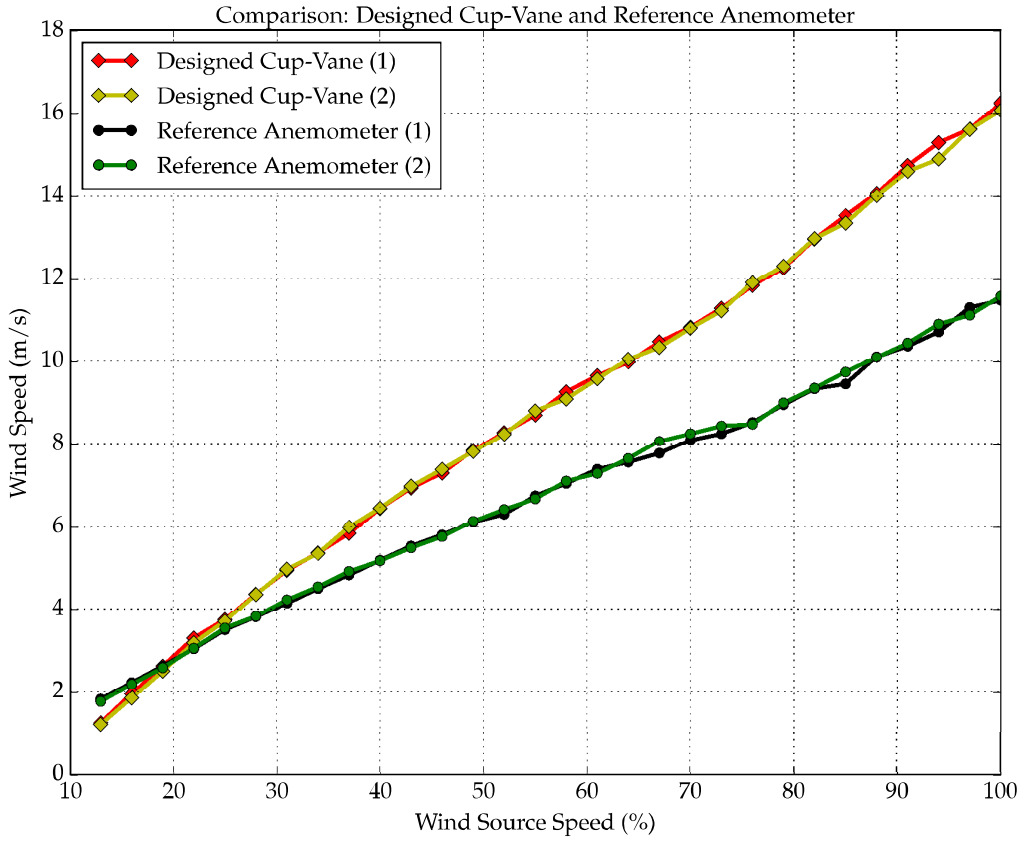

Figure 7. Designed cup-vane (not calibrated) vs. reference anemometer wind speed plot.

The wind source used (Armfield^{TM} C15 wind tunnel) expressed wind speed in terms of percentage. The comparison of Figure 7 is important in the sense that it shows that the data collected from the designed cup-vane instrument were linear and consistent. This made the calibration process much easier. Still, the relationship between the designed cup-vane instrument and the reference anemometer could be found easily. The next step was to perform the calibration. A graph of the designed cup-vane instrument RPM versus the reference anemometer tunnel wind speed was plotted. A polynomial function that best fits within the scatter plotted data was calculated and the results plotted using a Python program. This is shown in Figure 8.

To plot the trend line, the polyfit points were calculated. These data points are presented in Table A7. The correlation coefficient between the plotted points and the polynomial of best fit was also calculated. As seen in the plot of Figure 8, this relationship is linear. Most points fit within the trend line with an r-value of 0.9999999999999999 (approximately one). This means that the points fit within the calculated polynomial of best fit, and they are well above the recommended least r-value of 0.99995 [11]. This trend line is hence reliable.

To check further, the null hypothesis was used. In this case, the null hypothesis was that 'the scatter points had no relationship with the fitting polynomial'. After the calculation, the p-value returned $1.0597294907859924 \times 10^{-220}$, a value close to zero. This implied high confidence in rejecting the null hypothesis. The slope standard error was $1.8243130833413156 \times 10^{-9}$, also close to zero. This means that the calibration exercise returned positive results. The resulting speed transfer function for the designed cup-vane wireless sensor node instrument is as presented in Equation (1).

$$V[m/s] = 0.6478 \times CA[RPM] + 1.0164 \quad (1)$$

where $V[m/s]$ is the wind speed and $CA[RPM]$ is the designed cup RPM. Equation (1) is similar to the cup anemometer Equation (2).

$$V = Af + B \tag{2}$$

where A is the slope constant and B is the offset. Hence, the speed slope constant for the designed cup-vane instrument is 0.6478, while the offset is 1.0164.

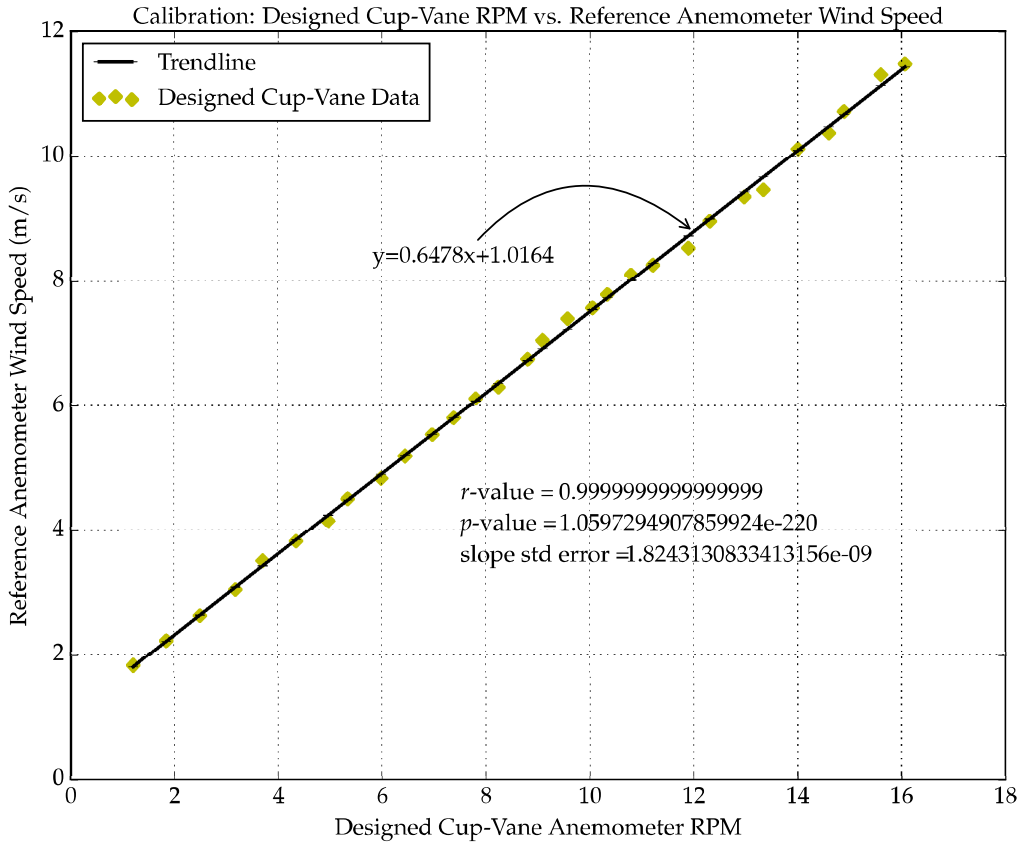

Figure 8. Designed cup-vane speed calibration graph.

4.3. Cup Calibration Uncertainty

The calculated uncertainty data output is shown in Table A2. The residual wind speed was plotted against the designed cup-vane RPM as shown in Figure 9. This plot illustrates that the developed cup-vane instrument had a maximum positive residual value (fitting deviation) of $+0.204084$ m/s, while the minimum was $+0.001048$ m/s. The maximum negative fitting deviation was -0.174730 m/s, while the minimum was -0.009122 m/s. The mean fitting deviation for positive and negative residuals was ± 0.063398 m/s.

After calibration, the calibrated cup-vane instrument and the reference anemometer were both exposed to wind from the wind tunnel at the same time, as seen in the setup of Figure 6. A comparison graph of the acquired calibrated data versus the data collected by the reference anemometer was then plotted as shown in Figure 10. It was observed that the designed cup-vane instrument presented reliable data after calibration. These data reflected the true wind speed.

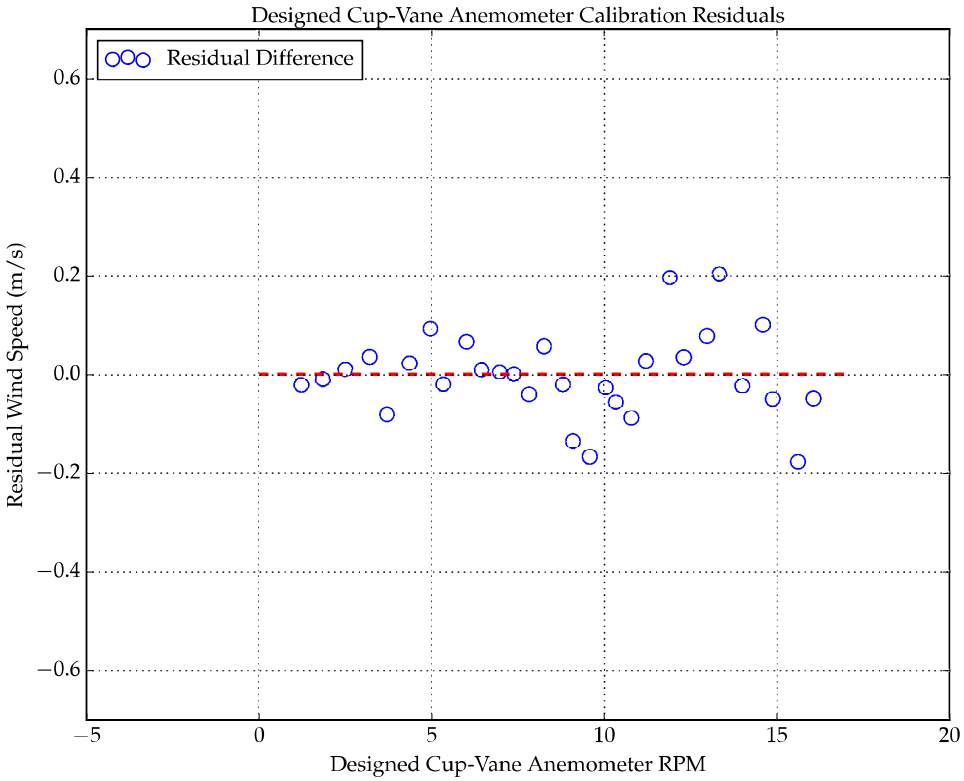

Figure 9. Designed cup-vane (calibrated) speed residuals graph.

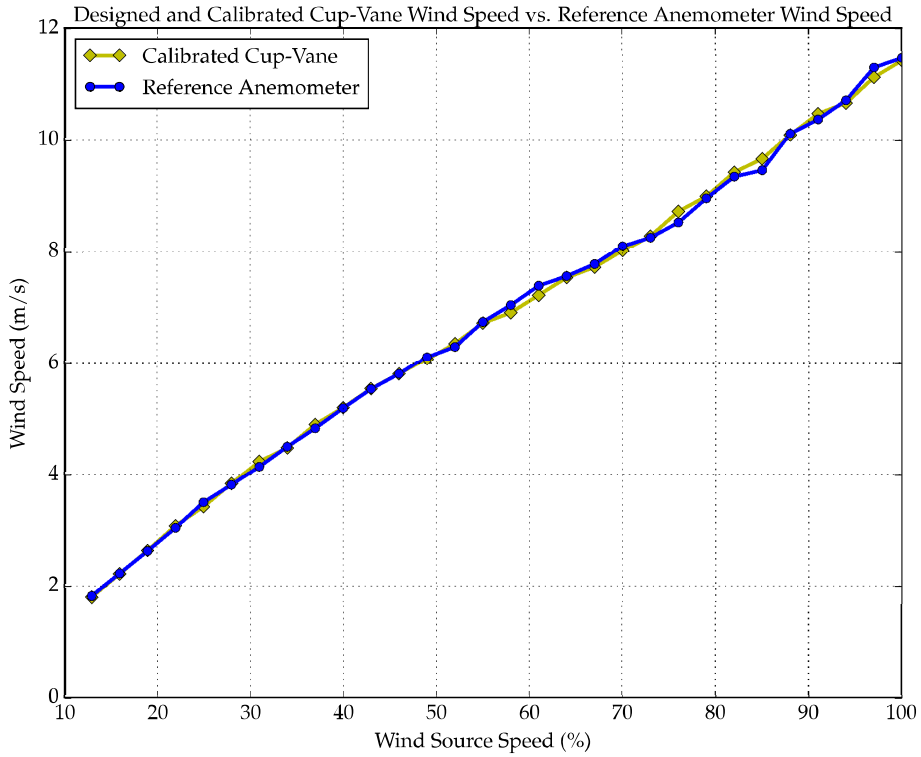

Figure 10. Designed cup-vane (calibrated) vs. reference anemometer wind speed measurements.

4.4. Cup Hysteresis Losses

As recommended by the IEC61400-12-1(2005) standards [11], the designed cup-vane instrument was checked for hysteresis losses. Wind data from the tunnel were collected as the wind source was varied from minimum to maximum (rising) and back from maximum to minimum (falling). The hysteresis data output is presented in Table A3. A graph for the rising and falling data was plotted on the same axis as illustrated in Figure 11. The results in this graph presented negligible levels of hysteresis loss.

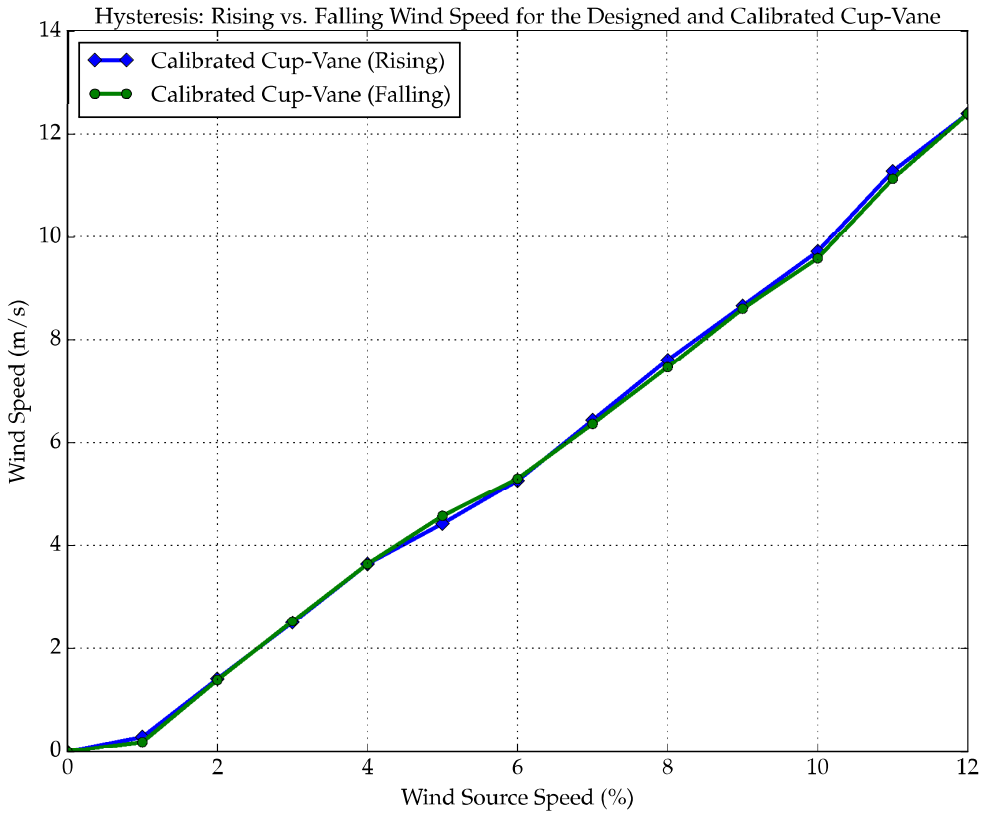

Figure 11. Designed cup-vane (calibrated) hysteresis losses graph.

4.5. Vane Calibration Setup

Before the vane compass sensor was put to work, it needed to be calibrated. The setup that was used for this exercise is shown in Figure A2 in Appendix A. This sensor uses the I^2C communication protocol. Python running on a Raspberry Pi 3 was used for this calibration exercise. As seen in the same Figure A2 , the HMC5883L sensor was mounted on a 360° slip ring connector to enable a free 360° rotation. In reference to the sensor datasheet [34] and other sources [35,36], a Python program was used for further sensor setup.

4.6. Vane Calibration Results and Analysis

To perform vane calibration, clockwise and counterclockwise vane sensor (HMC5883L) data were required. To gather clockwise data, the vane of the designed cup-vane instrument was rotated clockwise. Similarly, to collect counterclockwise data, the vane of the designed cup-vane instrument was rotated counterclockwise. The output plot for clockwise and counterclockwise data sets is shown in Figure 12. The counterclockwise data are presented in Table A4 From this plot, it can be seen that the data collected from the sensor was well represented throughout 360°. There was only one stray

data point, which was negligible. However, this representation clearly showed that the sensor data for both clockwise and counterclockwise were similar and offset.

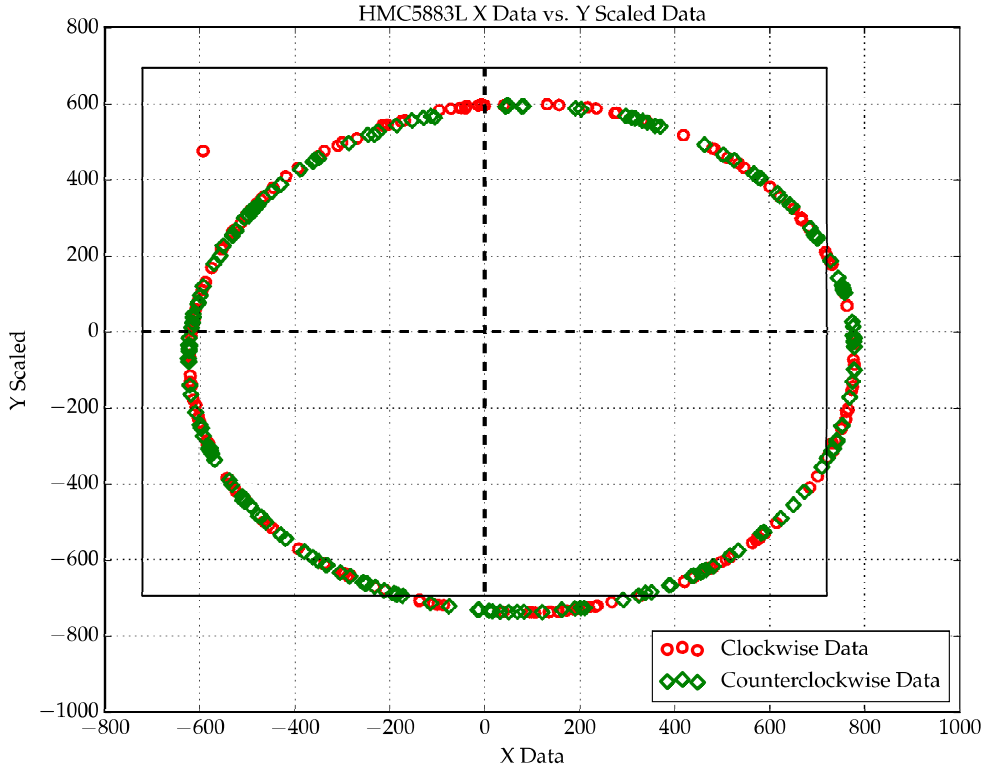

Figure 12. Designed cup-vane HMC5883L sensor clockwise and counterclockwise plot (not calibrated).

To correct the offset error, the offset amount was calculated using a Python program that captured the maximum and minimum data as the sensor was being rotated back and forth through 360 degrees. The program output presented the offsets as shown in Table 1. For offset compensation, the offset values were incorporated into the Python program formula, and data were collected again, as the vane sensor was rotated back and forth throughout 360°. Around 250 sets of data were collected and saved in a file. This is as presented in Table A5 Data collected before and after calibration were plotted on the same axes as before. The graphical results are shown in Figure 13.

Table 1. Offset output data.

minx:	−628
miny:	−814
maxx:	790
maxy:	662
x offset:	81
y offset:	−76

The final results show that after calibration, the HMC5883L offset was taken care of and data did fit well at the center, throughout 360° rotation. The last thing to factor in was the varying magnetic declination [37]. This was factored in the working algorithm.

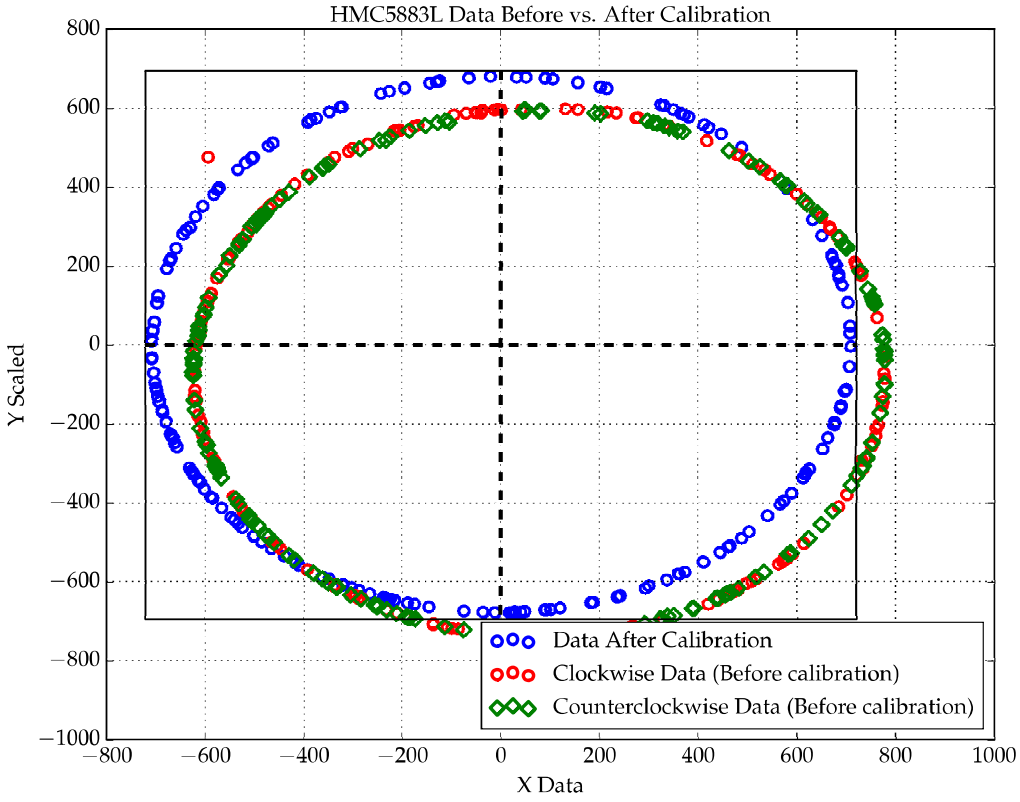

Figure 13. Designed cup-vane HMC5883L sensor clockwise and counterclockwise plot (after calibration).

5. Conclusions

This research gave rise to a wireless 3D-printed cup-vane instrument capable of transmitting wind data wirelessly via the IEEE 802.15.4 protocol into a central station located up to 100 m away. This implementation represents a sensor node capable of transmitting wind speed, wind direction, air temperature, air humidity, air pressure and altitude. More such instrument nodes can be installed at different points and made to transmit to the same central station via a wireless sensor network. This implementation makes wind data collection easy and cost-effective as compared to most commercial options.

The developed cup-vane was found to be governed by a specific speed calibration function presented by Equation (1). The designed cup-vane instrument mean fitting deviation for positive and negative residuals was ± 0.063398 m/s. This is as illustrated by the residuals results of Figure 9. The wind vane developed recorded an x-offset of 81 and a y-offset of -76. These offsets were corrected after calibration. This instrument has the potential to facilitate massive wind data collection, which is the grounds for rapid wind energy investment.

Author Contributions: Conceptualization, S.K. Data curation, C.G. Formal analysis, S.K. and C.G. Methodology, S.K. Supervision, J.B. and H.N. Validation, C.G. Writing, original draft, S.K. Writing, review and editing, C.G., J.B. and H.N.

Funding: This research received no external funding.

Acknowledgments: This research was carried out at Dedan Kimathi University of Technology (DeKUT, Kenya) Mechatronics Laboratory, which offered the equipment that was needed to carry out this research.

Conflicts of Interest: The authors declare no conflict of interest.

Appendix A. Photographs

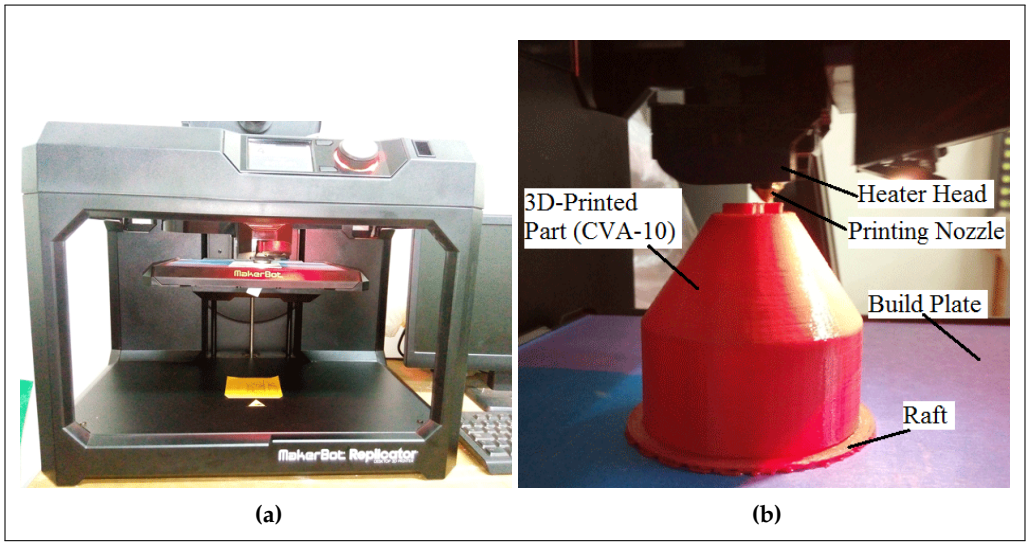

Figure A1. 3D printing setup: (**a**) setup and (**b**) printing process.

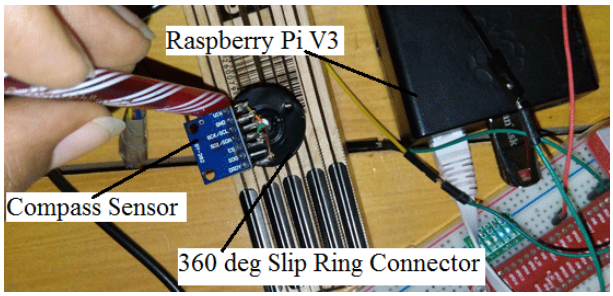

Figure A2. HMC5883L sensor calibration setup.

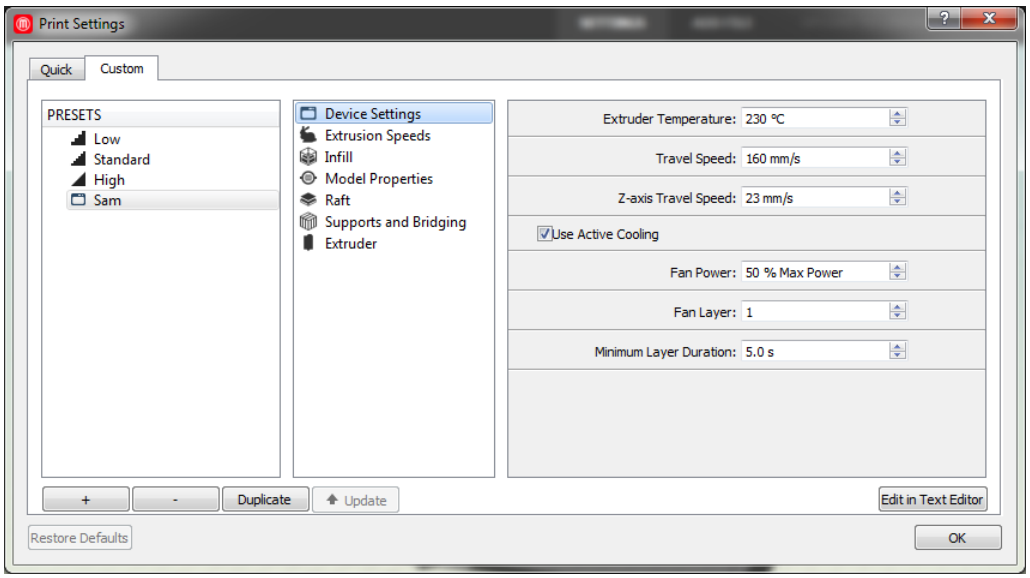

Figure A3. 3D printing parameter setting.

Appendix B. Sample Algorithm.

Algorithm A1

```
void loop()
{
time_now = millis();
newEncPos = encPos;
newtym = millis();
rpm = (newEncPos-oldEncPos) * 1000 /(newtym-oldtym);
if(rpm >= 0 || rpm <= 0)
{
Serial.print (rpm);
Serial.print(",");
}
oldEncPos = newEncPos;
oldtym = newtym;
```

Algorithm A2

```
Wire.beginTransmission(hmcAddr);
sensors_event_t event;
mag.getEvent(&event);
event.magnetic.x;
event.magnetic.y;
event.magnetic.z;
Wire.endTransmission();
float heading = atan2(event.magnetic.y, event.magnetic.x);
float declinationAngle = 0.22;
heading += declinationAngle;
if(heading < 0)
heading += 2*PI;
if(heading > 2*PI)
heading -= 2*PI;
float headingDegrees = heading * 180/M_PI;
Serial.print(headingDegrees);
Serial.print(",");
```

Algorithm A3

```
Wire.beginTransmission(bmpAddr);
Serial.print(bmp.readTemperature());
Serial.print(",");
Serial.print(bmp.readPressure());
Serial.print(",");
Serial.print(bmp.readAltitude());
Serial.println(",");
Wire.endTransmission();
while(millis() < time_now + period){}
}
```

Table A1. Designed Cup-Vane Wireless Sensor Node vs. Reference Anemometer Wind Speed Data.

Wind Source (%)	Designed Cup-Vane		Reference Anemometer	
	Run Round 1	Run Round 2	Run Round 1	Run Round 2
13	1.2614	1.2214	1.8286	1.7714
16	1.9586	1.8571	2.2286	2.1857
19	2.6286	2.5043	2.6286	2.5857
22	3.3043	3.1857	3.0429	3.0571
25	3.7471	3.7100	3.5000	3.5429
28	4.3657	4.3543	3.8143	3.8286
31	4.9400	4.9700	4.1429	4.2286
34	5.3629	5.3471	4.5000	4.5429
37	5.8343	5.9900	4.8286	4.9143
40	6.4414	6.4500	5.1857	5.1714
43	6.9343	6.9729	5.5286	5.4857
46	7.2943	7.3857	5.8000	5.7571
49	7.8414	7.8100	6.1143	6.1286
52	8.2843	8.2457	6.3000	6.4143
55	8.7071	8.8086	6.7429	6.6714
58	9.2671	9.0943	7.0429	7.1000
61	9.6529	9.5757	7.3857	7.2857
64	9.9800	10.0557	7.5571	7.6429
67	10.4729	10.3414	7.7714	8.0714
70	10.8286	10.8000	8.1000	8.2571
73	11.2814	11.2186	8.2571	8.4429
76	11.8257	11.9000	8.5286	8.4857
79	12.2671	12.3114	8.9571	9.0000
82	12.9614	12.9757	9.3429	9.3571
85	13.5271	13.3443	9.4571	9.7429
88	14.0671	14.0086	10.1143	10.1000
91	14.7386	14.6000	10.3714	10.4429
94	15.2914	14.8943	10.7143	10.9000
97	15.6171	15.6043	11.3000	11.1143
100	16.2471	16.0671	11.4714	11.5714

Table A2. Cup-Vane Wireless Sensor Node Wind Speed Uncertainty Data.

Reference Anemometer (m/s)	Designed Cup-Vane (m/s)	Residual (m/s)
1.8286	1.807656	−0.020944
2.2286	2.219478	−0.009122
2.6286	2.638751	0.010151
3.0429	3.080180	0.037280
3.5000	3.419835	−0.080165
3.8143	3.837229	0.022929
4.1429	4.236096	0.093196
4.5000	4.480391	−0.019609
4.8286	4.896878	0.068278
5.1857	5.194878	0.009178
5.5286	5.533626	0.005026
5.8000	5.801048	0.001048

Table A2. *Cont.*

Reference Anemometer (m/s)	Designed Cup-Vane (m/s)	Residual (m/s)
6.1143	6.075921	−0.038379
6.3000	6.358179	0.058179
6.7429	6.722840	−0.020060
7.0429	6.907924	−0.134976
7.3857	7.219787	−0.165913
7.5571	7.530744	−0.026356
7.7714	7.715827	−0.055573
8.1000	8.012920	−0.087080
8.2571	8.284100	0.027000
8.5286	8.725529	0.196929
8.9571	8.992044	0.034944
9.3429	9.422395	0.079495
9.4571	9.661184	0.204084
10.1143	10.091534	−0.022766
10.3714	10.474659	0.103259
10.7143	10.665314	−0.048986
11.3000	11.125270	−0.174730
11.4714	11.425084	−0.046316

Table A3. Cup-Vane Wireless Sensor Node Hysteresis Data.

Rising Wind Speed (m/s)	Falling Wind Speed (m/s)
0.000000	12.394286
0.285000	11.130000
1.406667	9.571250
2.500000	8.598571
3.640000	7.458333
4.420000	6.360000
5.262500	5.300000
6.430000	4.570000
7.601667	3.640000
8.654286	2.523333
9.705000	1.386667
11.277143	0.185000
12.394286	0.000000

Table A4. Cup-Vane Wireless Sensor Node Direction Data (HMC5883L) before Calibration.

X	Y	X Scaled	Y Scaled	Bearing
673	−457	619.16	−420.44	325.821573
778	−28	715.76	−25.76	357.938831
642	364	590.64	334.88	29.552291
342	598	314.64	550.16	60.234486
342	598	314.64	550.16	60.234486
−361	486	−332.12	447.12	126.604904
−570	194	−524.40	178.48	161.203948
−622	−54	−572.24	−49.68	184.961791
−532	−438	−489.44	−402.96	219.464909

Table A4. *Cont.*

X	Y	X Scaled	Y Scaled	Bearing
−532	−438	−489.44	−402.96	219.464909
−283	−700	−260.36	−644.00	247.987220
17	−800	15.64	−736.00	271.217352
351	−745	322.92	−685.40	295.227044
351	−745	322.92	−685.40	295.227044
351	−745	322.92	−685.40	295.227044
778	−107	715.76	−98.44	352.169117
700	270	644.00	248.40	21.092340
317	610	291.64	561.20	62.540357
317	610	291.64	561.20	62.540357
−224	573	−206.08	527.16	111.351769
−506	325	−465.52	299.00	147.287671
−603	84	−554.76	77.28	172.069534
−576	−341	−529.92	−313.72	210.626122
−576	−341	−529.92	−313.72	210.626122
⋮	⋮	⋮	⋮	⋮
754	125	693.68	115.00	9.413025
754	125	693.68	115.00	9.413025
525	491	483.00	451.72	43.083337
−106	613	−97.52	563.96	99.810575
−495	343	−455.40	315.56	145.280778
−622	−49	−572.24	−45.08	184.504352
−622	−49	−572.24	−45.08	184.504352
−580	−335	−533.60	−308.20	210.010138
−379	−630	−348.68	−579.60	238.969418
33	−801	30.36	−736.92	272.359166
33	−801	30.36	−736.92	272.359166
33	−801	30.36	−736.92	272.359166
730	−341	671.60	−313.72	334.961627
752	133	691.84	122.36	10.029711
621	388	571.32	356.96	31.997089
621	388	571.32	356.96	31.997089
45	644	41.40	592.48	86.002910
−490	350	−450.80	322.00	144.462322
−613	40	−563.96	36.80	176.266580
−597	−276	−549.24	−253.92	204.811646
−597	−276	−549.24	−253.92	204.811646
−470	−529	−432.40	−486.68	228.379909
−211	−740	−194.12	−680.80	254.085287
162	−795	149.04	−731.40	281.517676

Table A5. Cup-Vane Wireless Sensor Node Direction Data (HMC5883L) after Calibration.

X	Y	X Scaled	Y Scaled	Bearing
−348	642	−320.16	590.64	118.460176
−658	266	−605.36	244.72	157.988717
−701	−104	−644.92	−95.68	188.438817
−701	−104	−644.92	−95.68	188.438817
−625	−351	−575.00	−322.92	209.318567
−465	−562	−427.80	−517.04	230.395572
−239	−696	−219.88	−640.32	251.048000

Table A5. *Cont.*

X	Y	X Scaled	Y Scaled	Bearing
41	−736	37.72	−677.12	273.188453
41	−736	37.72	−677.12	273.188453
373	−626	343.16	−575.92	300.788458
626	−342	575.92	−314.64	331.351078
703	117	646.76	107.64	9.449105
703	117	646.76	107.64	9.449105
703	117	646.76	107.64	9.449105
−124	727	−114.08	668.84	99.679447
−506	516	−465.52	474.72	134.439394
−630	324	−579.60	298.08	152.783888
−630	324	−579.60	298.08	152.783888
−630	324	−579.60	298.08	152.783888
−687	−179	−632.04	−164.68	194.603897
−614	−372	−564.88	−342.24	211.210130
−362	−640	−333.04	−588.80	240.506414
−362	−640	−333.04	−588.80	240.506414
18	−738	16.56	−678.96	271.397181
⋮	⋮	⋮	⋮	⋮
−707	11	−650.44	10.12	179.108624
−707	11	−650.44	10.12	179.108624
−707	11	−650.44	10.12	179.108624
−485	−543	−446.20	−499.56	228.229218
−233	−697	−214.36	−641.24	251.515743
30	−735	27.60	−676.20	272.337306
30	−735	27.60	−676.20	272.337306
360	−631	331.20	−580.52	299.705752
675	−219	621.00	−201.48	342.024633
687	186	632.04	171.12	15.149212
687	186	632.04	171.12	15.149212
687	186	632.04	171.12	15.149212
105	732	96.60	673.44	81.837026
−391	614	−359.72	564.88	122.489303
−644	305	−592.48	280.60	154.657649
−644	305	−592.48	280.60	154.657649
−704	−77	−647.68	−70.84	186.241914
−609	−379	−560.28	−348.68	211.895313
−392	−619	−360.64	−569.48	237.654759
−75	−733	−69.00	−674.36	264.157871
−75	−733	−69.00	−674.36	264.157871
293	−671	269.56	−617.32	293.589051
589	−409	541.88	−376.28	325.223992
708	33	651.36	30.36	2.668635

Table A6. Cup-Vane Wireless Sensor Node Collected Data Sample.

Time (s)	Speed (m/s)	Direction (deg)	Temp. (°C)	Pressure (Pa)	Altitude (m)	Humidity (%)
500	1.00	341.28	27.2	82,266	1723.46	37
505	1.13	340.55	27.2	82,263	1723.75	35
510	1.07	340.06	27.2	82,268	1723.46	53
515	1.88	340.37	27.2	82,268	1723.46	51
520	2.03	340.51	27.3	82,262	1723.66	50
525	1.86	341.39	27.3	82,257	1723.36	41
530	1.72	339.31	27.3	82,257	1724.15	40
535	1.57	337.09	27.3	82,254	1725.43	39
540	2.84	11.78	27.3	82,249	1724.15	38
545	3.80	35.14	27.3	82,255	1724.74	36
550	3.90	46.30	27.3	82,254	1724.94	52
555	2.88	112.41	27.3	82,253	1724.35	51
560	2.19	341.32	27.4	82,257	1724.74	38
565	2.60	342.86	27.4	82,260	1724.15	36
570	0.72	345.31	27.5	82,265	1723.36	46
575	1.88	214.41	27.5	82,262	1723.95	41
580	2.77	345.04	27.5	82,264	1723.36	40
585	1.97	345.33	27.5	82,263	1723.85	39
590	2.32	343.20	27.5	82,265	1724.25	38
595	1.62	344.91	27.5	82,264	1723.66	36
600	1.45	345.00	27.5	82,267	1723.16	52
605	2.50	345.11	27.5	82,273	1722.87	52
610	1.66	344.21	27.5	82,271	1722.97	51
615	1.55	344.48	27.5	82,274	1723.06	50
⋮	⋮	⋮	⋮	⋮	⋮	⋮
885	2.86	345.93	27.8	82,262	1723.26	41
890	1.67	344.42	27.8	82,266	1723.75	40
895	1.70	340.85	27.9	82,263	1724.35	52
900	1.20	341.13	27.9	82,272	1723.75	46
905	1.65	343.07	27.9	82,266	1723.06	39
910	1.79	343.30	27.9	82,266	1723.16	38
915	1.75	343.25	27.9	82,268	1723.26	36
920	0.77	345.03	27.9	82,267	1722.87	35
925	0.54	337.47	27.9	82,263	1723.56	52
930	0.71	344.89	28.0	82,261	1723.36	52
935	0.44	344.81	28.0	82,268	1723.75	51
940	0.33	345.69	28.0	82,265	1723.36	50
945	0.69	343.34	28.0	82,266	1723.26	49
950	1.28	344.57	28.0	82,274	1722.97	44
955	1.28	344.52	28.0	82,266	1723.06	36
960	0.84	344.16	28.0	82,270	1722.47	53
965	1.24	342.39	28.1	82,265	1723.06	52
970	1.48	344.67	28.1	82,269	1723.16	52
975	1.40	343.55	28.1	82,272	1723.66	51
980	1.16	337.07	28.1	82,269	1723.66	50
985	0.97	344.89	28.1	82,267	1723.75	49
990	0.77	344.63	28.1	82,260	1723.06	47
995	0.80	341.14	28.1	82,265	1723.56	44

Table A7. Polyfit Calibration Data.

X-Axis Polynomial Fitting Data	Y-Axis Polynomial Fitting Data
1.2214	1.807656
1.8571	2.219478
2.5043	2.638751
3.1857	3.080180
3.7100	3.419835
4.3543	3.837229
4.9700	4.236096
5.3471	4.480391
5.9900	4.896878
6.4500	5.194878
6.9729	5.533626
7.3857	5.801048
7.8100	6.075921
8.2457	6.358179
8.8086	6.722840
9.0943	6.907924
9.5757	7.219787
10.0557	7.530744
10.3414	7.715827
10.8000	8.012920
11.2186	8.284100
11.9000	8.725529
12.3114	8.992044
12.9757	9.422395
13.3443	9.661184
14.0086	10.091534
14.6000	10.474659
14.8943	10.665314
15.6043	11.125270
16.0671	11.425084

References

1. Hoel, M.; Kverndokk, S. Depletion of fossil fuels and the impacts of global warming. *Sci. Resour. Energy Econ.* **1996**, *18*, 115–136. [CrossRef]
2. Fried, L. *Global Wind Statistics 2017*; Technical Report; GWEC: Brussels, Belgium, 2017.
3. LTWP. Lake Turkana Wind Power. 2016. Available online: https://ltwp.co.ke/ (accessed on 1 May 2018).
4. Wikipedia Contributors. Wind Power in Kenya—Wikipedia, The Free Encyclopedia. 2017. Available online: https://en.wikipedia.org/w/index.php?title=Wind_power_in_Kenya&oldid=797403118 (accessed on 2 May 2018).
5. Henry, W. *Anemometer*; Encyclopædia Britannica:Chicago, IL, USA, 1911.
6. Middleton, W.K. *Invention of the Meteorological Instruments*; The Johns Hopkins Press: Baltimore, MA, USA, 1969.
7. Middleton, W.K.; Spilhaus, A.F. *Meteorological Instruments*, 3rd ed.; University of Toronto Press: Toronto, ON, Canada, 1953.
8. Gasch, P.D.I.R.; Twele, P.D.I.J. *Wind Power Plants: Fundamentals, Design, Construction and Operation*, 2nd ed.; Springer: Berlin/Heidelberg, Germany, 2012.
9. Hunter, R.S. *Recommended Practices for Wind Turbine Testing, Part 11. Wind Speed Measurement and Use of Cup Anemometry*; Technical Report; International Energy Agency: Denmark, 2003. Available online: https://community.ieawind.org/HigherLogic/System/DownloadDocumentF (accessed on 2 June 2018).
10. Pindado, S.; Cubas, J.; Sorribes-Palmer, F. The Cup Anemometer, a Fundamental Meteorological Instrument for the Wind Energy Industry. *Energies* **2014**, *14*, 21418–21452.
11. Standard, I.E.C. *Part 12-1: Power Performance Measurements of Electricity Producing Wind Turbines*, 1st ed.; IEC: Geneva, Switzerland, 2005.
12. Kristensen, L. The Perennial Cup Anemometer. *Wind Energy* **1999**, *2*, 59–75. [CrossRef]

13. Ammonit. *Data Logger Meteo-40 User Manual*; Ammonit Measurement GmbH: Berlin, Germany, 2012; pp. 2–77.
14. Kristensen, L. Fragments of the Cup Anemometer History. *Wind Sens.* **2005**. Available online: https://www.windsensor.com/application/files/9115/1721/7060Fragments_of_The_Cup_Anemometer_History_20050214.pdf (accessed on 10 May 2018).
15. Kristensen, L.; Hansen, O.F.; Hansen, S.O. The Working of the Cup Anemometer. *Wind Sens.* **2014**, *2*, 1–18.
16. Wieringa, J. Evaluation and Design of Wind Vanes. *J. Appl. Meteorol.* **1967**, *6*, 1114–1122. [CrossRef]
17. Kerhascoët, H.; Laurent, J.; Cerqueus, A.; Sevaux, M.; Senn, E.; Hauville, F.; Coneau, R. Methodology for optimal wind vane design. In Proceedings of the OCEANS 2016, Shanghai, China, 10–13 April 2016.
18. Hsiao, C.C.; Jhang, J.W.; Siao, A.S. Study on Pyroelectric Harvesters Integrating Solar Radiation with Wind Power. *Energies* **2015**, *8*, 7465–7477, doi:10.3390/en8077465. [CrossRef]
19. Mpofu, T.P.; Mawere, C.; Mukosera, M. The Impact and Application of 3D Printing Technology. *Int. J. Sci. Res. IJSR* **2014**, *3*, 2148–2150.
20. Thryft, A.R. 3D Printing Will (Eventually) Transform Manufacturing. Available online: http://www.designnews.com/author.asp?doc_id=262205&dfpPParams=ind_183,industry_auto,industry_aero,industry_consumer,industry_machinery,industry_medical,bid_27,aid_262205&dfpLayout=blog (accessed on 18 June 2018).
21. Xu, Y.; Wu, X.; Guo, X.; Kong, B.; Zhang, M.; Qian, X.; Mi, S.; Sun, W. The Boom in 3D-Printed Sensor Technology. *Sensors* **2017**, *17*, 1166. [CrossRef] [PubMed]
22. A.T.Kearney. *3D Printing: A Manufacturing Revolution*; Technical report; A.T.Kearney: Chicago, IL USA, 2015.
23. Paritalaa, P.K.; Manchikatlab, S.; Yarlagadda, P. Digital Manufacturing-Applications Past, Current, and Future Trends. *Procedia Eng.* **2017**, *174*, 982–991. [CrossRef]
24. Pereira, O.; Rodríguez, A.; Barreiro, J.; Isabel, A.; Norberto, L. Nozzle design for combined use of MQL and cryogenic gas in machining. *Korean Soc. Precis. Eng.* **2017**, *4*, 87–95, doi:10.1007/s40684-017-0012-3. [CrossRef]
25. Adane, A.; Yahia, A.A.; Mameri, E.; Adane, A.E.H. Design of a Microcontroller-Based Data Acquisition System for Ground Weather Observations: Evaluation of Radio Refractivity of Air. *Int. J. Commun. Netw. Syst. Sci.* **2014**, *7*, 355–364. [CrossRef]
26. Chauhan, N.; Kumar, R. Data Acquisition System. *IJIRT* **2014**, *1*, 973–976.
27. Koutroulis, E.; Kalaitzakis, K. Development of an integrated data-acquisition system for renewable energy sources systems monitoring. *Renew. Energy* ***2003***, 28, *139–152*. [CrossRef]
28. Nguyen, C.D.; Tran, T.D.; Tran, N.D.; Huynh, T.H.; Nguyen, D.T. Flexible and Efficient Wireless Sensor Networks for Detecting Rainfall-Induced Landslides. *Int. J. Distrib. Sens. Netw.* **2015**, *11*, 235954. [CrossRef]
29. Gahlot, N.; Gundkal, V.; Kothimbire, S.; Thite, A. Zigbee based weather monitoring system. *Int. J. Eng. Sci. IJES* **2015**, *4*, 61–66.
30. SriLakshmi, P.; Das, N.L.; Manikumar, C. Low-cost wireless instrumentation for monitoring humidity, wind speed, and direction. *Instrum. Sci. Technol.* **2017**, *45*, 479–485. [CrossRef]
31. Omron. *Incremental 60-Mm-Dia. 360P/R Rotary Encoder Datasheet*; Technical Report; Omron Electronics LLC: Hoffman Estates, IL, USA, 2015.
32. Freitag, H.; O'Haleck, M.; Thomas, G.; McPhaden, M. *Calibration Procedures and Instrumental Accuracies for ATLAS Wind Measurements*; Technical Report; NOAA/Pacific Marine Environmental Laboratory: Seattle, WA, USA, 2001.
33. Measnet. *Anemometer Calibration Procedure Version 2*; Technical report; Measnet: Madrid, Spain, 2009.
34. Honeywell. *3-Axis Digital Compass IC HMC5883L Datasheet*; Technical Report; Honeywell: Plymouth, MN, USA, 2011.
35. Bitify. *Connecting and Calibrating a HMC5883L Compass on the Raspberry Pi*; Bitify: Newport, Australia, 2013.
36. Instructables, A. Configure, Read Data and Calibrate the HMC5883L Digital Compass Using Python. 14 July 2015. Available online: http://www.instructables.com/id/Configure-read-data-calibrate-the-HMC5883L-digital/ (accessed on 21 June 2018).
37. Declination, M. Magnetic Declination. 2018. Available online: http://www.magnetic-declination.com/ (accessed on 1 May 2018).